Journal of Crystal Growth 135 (1994) 341–353
North-Holland

JOURNAL OF CRYSTAL GROWTH

Macrosegregation and convection in the horizontal Bridgman configuration I. Dilute alloys

S. Kaddeche, H. Ben Hadid and D. Henry

Laboratoire de Mécanique des Fluides et d'Acoustique, URA CNRS 263, Ecole Centrale de Lyon / Université Claude Bernard – Lyon 1, ECL-BP 163, F-69131 Ecully Cedex, France

Received 1 May 1993; manuscript received in final form 16 September 1993

Numerical studies of macrosegregation in the horizontal Bridgman configuration for a rectangular cavity filled with a dilute low Prandtl alloy are performed by investigating the flow structures and the species distributions under various conditions. Two configurations are studied: buoyancy-driven convection in confined cavity (rigid–rigid case) and surface tension-driven flow in a cavity where the upper boundary is a free surface (rigid–free case). The effects of the Grashof, the Reynolds Marangoni and the Schmidt numbers are described for an aspect ratio $A = 4$ ($A = L/H$, where L is the length and H is the height of the cavity), a segregation coefficient $k = 0.087$ (corresponding to an alloy of Ge–Ga or GaAs–In), a growth rate $V_f = 2.7\ 10^{-5}$ m/s and a Prandtl number $\mathrm{Pr} = 0.015$. All the results are shown when half of the cavity is solidified. Particular attention is focused on understanding the influence of a transverse magnetic field on the flow structure and on the dopant distribution. One important feature of the action of the magnetic field is that strong magnetic field ($\mathrm{Ha} \geq 200$) has a significant effect in reducing radial segregation while intermediate values enhance the segregation effect.

1. Introduction

The purpose of this paper is to emphasize the role of buoyancy and thermocapillary-driven convection on macrosegregation in reduced gravity environment.

A survey of the literature indicates that for some simple geometries, analytic solutions to the transport equations are possible. The well-known expressions describing the limiting cases of solute distribution in the liquid (i.e. diffusion controlled solute transport and complete mixing) are those of Smith et al. [1] and Scheil [2], respectively. Favier [3,4] solved the one-dimensional solute conservation equation by considering a stagnant film model and gave the expression of the longitudinal dopant segregation in the crystal for a wide range of experimental conditions. Some other expressions for situations with partial mixing are reviewed by Camel and Favier [5,6]. Verhoeven et al. [7,8] solved numerically the one-dimensional diffusion equation and investigated the validity of the analytical solutions, namely that of Smith et al. [1] and Scheil [2].

Numerical investigations for different growth configurations are available in the literature. Chang and Brown [9] and Adornato and Brown [10] carried out large computations for vertical Bridgman cavity with deformable crystal–melt interface, first for dilute alloys [9] and then for both dilute and concentrated alloys [10]. Nikitin et al. [11] studied macrosegregation in horizontal Bridgman configuration for planar crystal–melt interface and moderate Grashof numbers ($\mathrm{Gr} \leq 5000$) corresponding to microgravity environment. They estimated numerically the longitudinal segregation and proved that the radial segregation has a maximum for intermediate Grashof number values.

The magnetic field is known for its effects to damp the velocity field and to stabilize both flow and temperature oscillations in the melt (see a

SSDI 0022-0248(93)E0324-Z

review paper of Series and Hurle [12]) and thereby represents a promising opportunity to obtain improved crystals quality. Mihelčić and Wingerath [13] proved through their numerical investigations that external axi-symmetric magnetic field can be used to damp velocity vectors and also to eliminate strong flow and temperature oscillations in the Czochralski growth configuration. Kim et al. [14] have conducted numerical simulations to study the effect of a vertically-aligned magnetic field on the growth processes in a vertical Bridgman configuration. Kim et al. [14] have proved that strong magnetic fields supress flow recirculation completely and lead to a quasi-diffusive regime (uniform solute segregation across the crystal).

In the following sections, macrosegregation is first studied for buoyancy-driven convection in a confined cavity (i.e., $Gr > 0$ and $Re = 0$). Dopant distribution for pure thermocapillary-driven flow (i.e., $Re > 0$ and $Gr = 0$) in a cavity with a flat free surface is then considered. In the last section, we investigate the influence of a constant magnetic field on such developed flows and its consequence on segregation.

2. Mathematical model

2.1. Governing equations

We consider a rectangular finite cavity of height H and length L (see fig. 1; $A = L/H$ is the aspect ratio), filled with a low Prandtl-number fluid of negligible electrical resistivity. The upper horizontal boundary can be rigid, or free and subject to a surface tension gradient. The fluid is assumed to be Newtonian with constant physical properties except for the density which obeys the Boussinesq approximation. The flow developed in the fluid, due to the horizontal thermal gradient resulting from differentially heated side walls, is assumed to be laminar. We also assume that the solid–liquid interface is planar and moving at a constant velocity V_f. The segregation coefficient k is constant and equal to its equilibrium value. Thus, along the solid/liquid interface, the crystal concentration is estimated

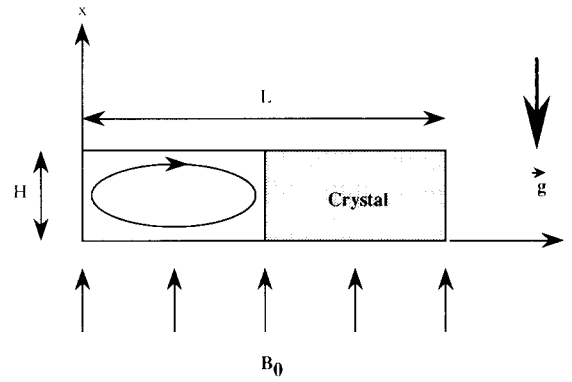

Fig. 1. Cavity configuration.

from the following formula: $C_S = k\, C_\ell$ (the subscripts s and l denote respectively the solid and the liquid phase). The surface tension on the free upper boundary is a linear function of temperature and is given by the following relationship: $\sigma = \sigma_0[1 - \gamma(T - T_0)]$, where $\gamma = -\sigma_0^{-1}\partial\sigma/\partial T$. We also assume that the magnetic Prandtl number $Pr_m = \chi\mu\mu_0\nu$ (χ is the electrical conductivity, $\mu\mu_0$ is the magnetic permitivity and ν is the kinematic viscosity of the melt) is sufficiently small to neglect the induced magnetic field with respect to the imposed constant transverse magnetic field B_0. With this assumption the current density vector reads as follows:

$$\boldsymbol{j} = \chi(\boldsymbol{E} + \boldsymbol{v} \wedge \boldsymbol{B}_0).$$

Assuming that the electrical field is negligible, the Lorentz force may be written:

$$\boldsymbol{f} = \chi(\boldsymbol{v} \wedge \boldsymbol{B}_0) \wedge \boldsymbol{B}_0.$$

The conservation equations of momentum, heat and species are made dimensionless using H^2/ν, ν/H, H, ∇TH and C_0 as scale quantities for time, velocity, length, temperature (∇T is the constant temperature gradient imposed by the heating facility) and concentration respectively. The dimensionless temperature is defined as $\theta = (T - T_c)/\nabla TH$, where T_c is the temperature of the interface. The domain containing the melt which varies during the solidification process is transformed into a fixed one using the following transformation: $y^* = y/S(x, t)$ and $x^* = x$ where $S(x, t)$ is the dimensionless length of the liquid

area. According to these transformations and after the elimination of the asterisk *, the dimensionless governing equations in the melt may be written in a vorticity-stream-function formulation as:

$$\frac{\partial\zeta}{\partial t}+u\frac{\partial\zeta}{\partial x}+(v-yv_f)\frac{1}{S}\frac{\partial\zeta}{\partial y}=\left(\frac{\partial^2\zeta}{\partial x^2}+\frac{1}{S^2}\frac{\partial^2\zeta}{\partial y^2}\right)-\mathrm{Gr}\frac{1}{S}\frac{\partial\theta}{\partial y}-\mathrm{Ha}^2\frac{\partial v}{\partial x}, \quad (1)$$

$$\left(\frac{\partial^2\psi}{\partial x^2}+\frac{1}{S^2}\frac{\partial^2\psi}{\partial y^2}\right)=-\zeta, \quad (2)$$

$$\frac{\partial\theta}{\partial t}+u\frac{\partial\theta}{\partial x}+(v-yv_f)\frac{1}{S}\frac{\partial\theta}{\partial y}=\frac{1}{\mathrm{Pr}}\left(\frac{\partial^2\theta}{\partial x^2}+\frac{1}{S^2}\frac{\partial^2\theta}{\partial y^2}\right), \quad (3)$$

$$\frac{\partial c}{\partial t}+u\frac{\partial c}{\partial x}+(v-yv_f)\frac{1}{S}\frac{\partial c}{\partial y}=\frac{1}{\mathrm{Sc}}\left(\frac{\partial^2 c}{\partial x^2}+\frac{1}{S^2}\frac{\partial^2 c}{\partial y^2}\right), \quad (4)$$

where v_f is the dimensionless interface velocity ($v_f = HV_f/\nu$). The dimensionless parameters appearing in eqs. (1)–(4), are the Grashof number $\mathrm{Gr} = g\beta\nabla T H^4/\nu^2$ (β is the volumic thermal expansion coefficient), the Prandtl number $\mathrm{Pr} = \nu/\kappa$, the Schmidt number $\mathrm{Sc} = \nu/D$ (D is the dopant diffusivity) and the Hartmann number $\mathrm{Ha} = B_0 H\ (\chi/\rho\nu)^{1/2}$. Note that in eq. (3), the viscous dissipation and the Joule heating are neglected.

2.2. Boundary conditions

– At the vertical rigid boundary, $y = 0$: $u = v = 0$, $\partial c/\partial y = 0$ and $\theta = S$.

– At the crystal–melt interface, $y = 1$: $u = v = 0$, $\theta = 0$, and the rate of solute rejected into the melt is given by

$$S^{-1}\,\partial c/\partial y = (1-k_0)\,\mathrm{Sc}\,v_f c. \quad (5)$$

– At the horizontal rigid boundary, $x = 0$: $u = v = 0$, $\partial c/\partial x = 0$, and for the temperature a linear profile is maintained corresponding to the temperature gradient imposed by the heating facility.

– At the upper boundary, $x = 1$:

For the rigid–rigid case : $u = v = 0$, $\partial c/\partial x = 0$, and for the temperature a linear profile as for $x = 0$.

For the rigid–free case: $u = 0$, $\partial c/\partial x = 0$, $\partial\theta/\partial x = 0$ and $\partial v/\partial x = -S^{-1}\,\mathrm{Re}\,\partial\theta/\partial y$, where Re is the Reynolds Marangoni number

$$\mathrm{Re} = -\frac{\partial\sigma}{\partial T}\nabla T\frac{H^2}{\rho\nu^2}. \quad (6)$$

2.3. Numerical procedure

The governing equations (1)–(4) are solved using an ADI (alternating direction implicit) technique with a finite-difference method involving forward differences for time derivatives and Hermitian relationships for spatial derivatives with a truncation error of $O(\Delta t^2, \Delta x^4, \Delta y^4)$ (see Hirsh [15] and Roux et al. [16]).

The mesh used to solve the problem (1)–(4) is generated by the Thompson technique [17]. We use a 25×101 grid which proved to give sufficiently accurate results for such studies (Ben Hadid [18]). Horizontally (in the y direction), the nodes are constricted by the side walls and especially by the interface while in the vertical direction the grid is symmetric with the nodes crowded near the horizontal side walls.

3. Results

The results are presented by the plot of the streamlines in the liquid phase and the iso-value lines of the dopant concentration in the crystal and in the melt. In order to investigate the influence of the melt motion on the segregation, we use the following variables:

$$cs_{av} = \int_0^1 c_s(x, S)\,\mathrm{d}x,$$

$$\Delta c = \frac{cs_{max}(x, S) - cs_{min}(x, S)}{cs_{av}},$$

as the diagnostic indicators for the longitudinal and the radial segregation along the crystal axis. Since we are interested in melt grown crystal in reduced gravity environment, we have considered the following parameter values: $Gr \leq 5000$ and $Re \leq 6666$ which match the reduced gravity environment conditions. Further, we have considered $1 \leq Sc \leq 100$ and $Pr = 0.015$. As Pr is very small, corresponding to strongly conducting materials, the temperature field is in all cases perfectly conducting with a constant horizontal gradient everywhere in the cavity.

3.1. Confined cavity: rigid–rigid case

In order to show the effects of the convective fluid motion on the dopant repartition, the concentration fields for two values of the Grashof number, $Gr = 10$ and 5000, and three values of the Schmidt number, $Sc = 10$, 50 and 100, are displayed in fig. 2. From this figure, for low Sc values ($Sc = 10$), it is clear, that when the flow is relatively weak (i.e., $Gr = 10$), the iso-concentration lines in the melt are almost vertical and the mass transfer is mainly achieved by diffusion, while for higher values of the Grashof number (i.e., $Gr = 5000$), the iso-concentration lines are more distorted. For this last case, two distinct regions are apparent in the melt zone: an enriched solute boundary layer near the crystal–melt interface (the extent of this layer decreases when increasing the Grashof number), and an area where the dopant concentration is nearly uniform especially when the Grashof number is important. This behaviour is mainly due to a higher level of flow convection which encloses the dopant rejected by the crystal near the growth interface and distributes it quite uniformly in the melt.

Fig. 2 also shows that for a given Grashof number and a Schmidt number varying from 10 to 100, the solute boundary layer extent in the melt decreases. For low Gr ($Gr = 10$), the solute boundary layer is reduced as Sc increases because the diffusion becomes dominated by the horizontal flow in the roll, but is not really affected by the vertical flow along the interface and is then almost uniform in depth. For stronger Gr ($Gr = 5000$), the solute boundary layer is less uniform in depth. Indeed, it is a little larger near the upper rigid wall where the no slip condition holds, and

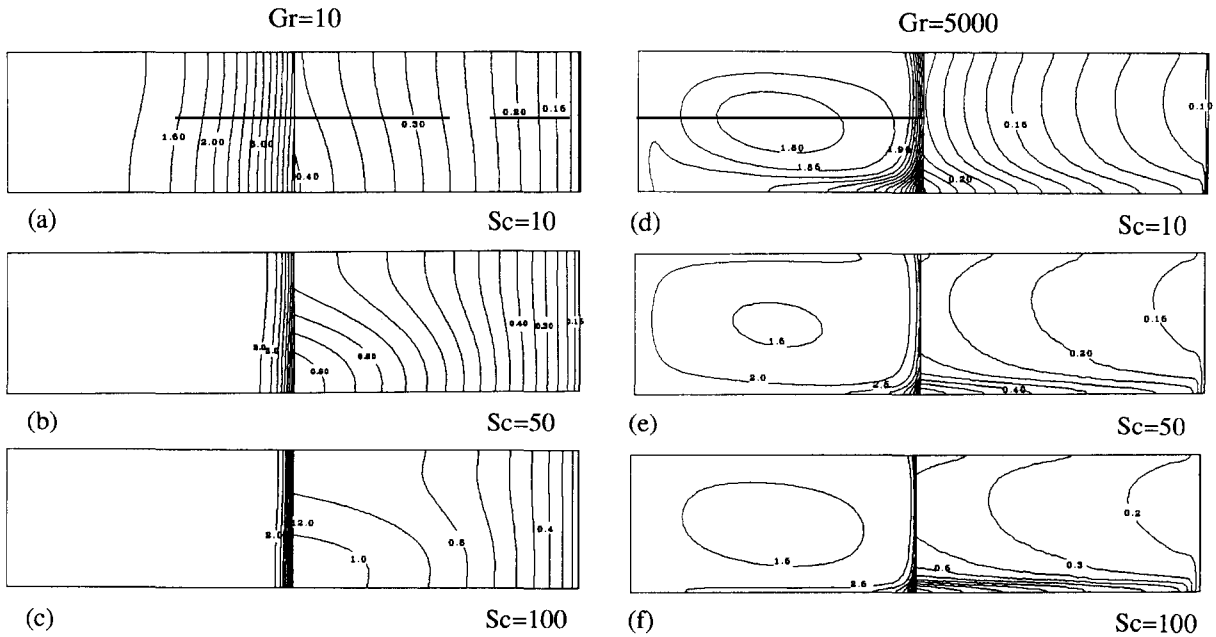

Fig. 2. Iso-concentration lines for $Gr = 10$, $Gr = 5000$ and different Schmidt numbers.

mainly increasing near the bottom where an enriched zone is formed through the descending flow along the interface.

As a consequence, for low Gr and Sc numbers (Gr = 10, Sc = 10), the concentration in the crystal almost corresponds to a diffusion-controlled transport regime with a weak radial segregation (compare with fig. 11e). When the Grashof number is increased, a zone enriched in dopant with increasing vertical concentration gradients is created at the bottom of the crystal, and is more and more pronounced as Sc is increased resulting in a strong radial segregation.

The curves giving the evolution of the longitudinal segregation along the crystal axis are displayed in fig. 3 for Sc = 10 and are compared with the analytical solutions for the two limiting regimes: the diffusion-controlled regime given by the formula of Smith et al. [1] and the well-mixed regime given by that of Scheil [2]. We first notice that the two limiting regimes compare favourably with the numerical results. Fig. 3 further shows that a different behaviour exists between the curves corresponding to the weak values of Grashof number (Gr = 10, Gr = 100) and those for higher values of Grashof number (Gr = 1000, Gr = 5000), reflecting the influence of buoyancy-driven convection on segregation.

Thus, buoyancy-driven convection influences both the quantity of dopant contained in the crystal and its compositional uniformity.

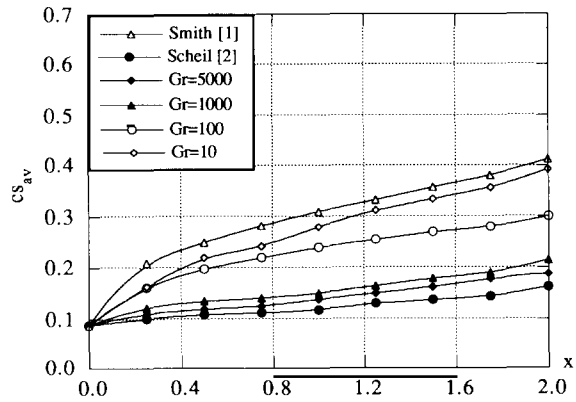

Fig. 3. Evolution of the longitudinal segregation along the crystal axis for Sc = 10 and different Grashof numbers.

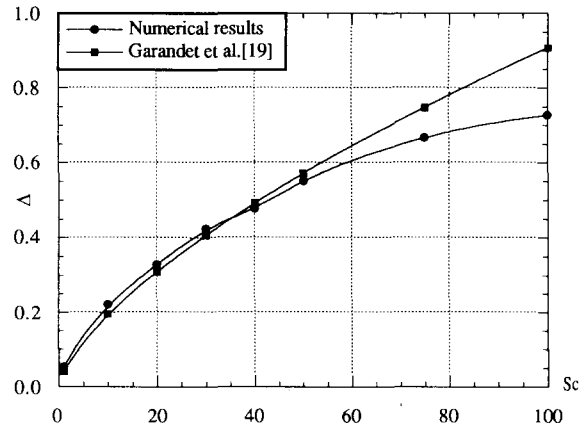

Fig. 4. Evolution of the reduced solute boundary layer Δ, as a function of the Schmidt number, for Gr = 5000.

The solute boundary layer extent is now investigated through the estimation of the parameter Δ_{SF} used by Favier [3,4]. The values of this parameter are obtained by adjusting the longitudinal segregation profiles given by the analytical relationships derived from Favier [3,4] to the segregation profiles obtained from the numerical simulations. The values of the dimensionless solute boundary layer extent $\Delta = \delta/\delta_d$ are then obtained through those of Δ_{SF}. Indeed, these two parameters are linked through the following relationship (see ref. [19]):

$$\Delta = 1 - \exp(-\Delta_{SF}). \tag{7}$$

The results obtained for Gr = 5000 are compared in fig. 4 to those of Garandet et al. [19] who used an order of magnitude analysis to estimate the dimensionless solute boundary layer extent and found in the developed convective regime that $\Delta = 3.6\mathrm{Pe}(\mathrm{Gr}\,\mathrm{Sc})^{-1/3}$. We may notice, referring to fig. 4, that our results compare favourably with those of Garandet et al. [19]. The maximum difference in the range of $1 \leq \mathrm{Sc} \leq 100$ is of the order of 20% for Sc = 100 indicating that the scaling law may have an other expression for $\mathrm{Sc} \geq 50$. Supplementary analogous investigations for Gr = 1000 have confirmed that the solute boundary layer thickness δ varies with respect to $\mathrm{Sc}^{-1/3}$ for a certain range of Schmidt numbers as predicted by Garandet et al. [19].

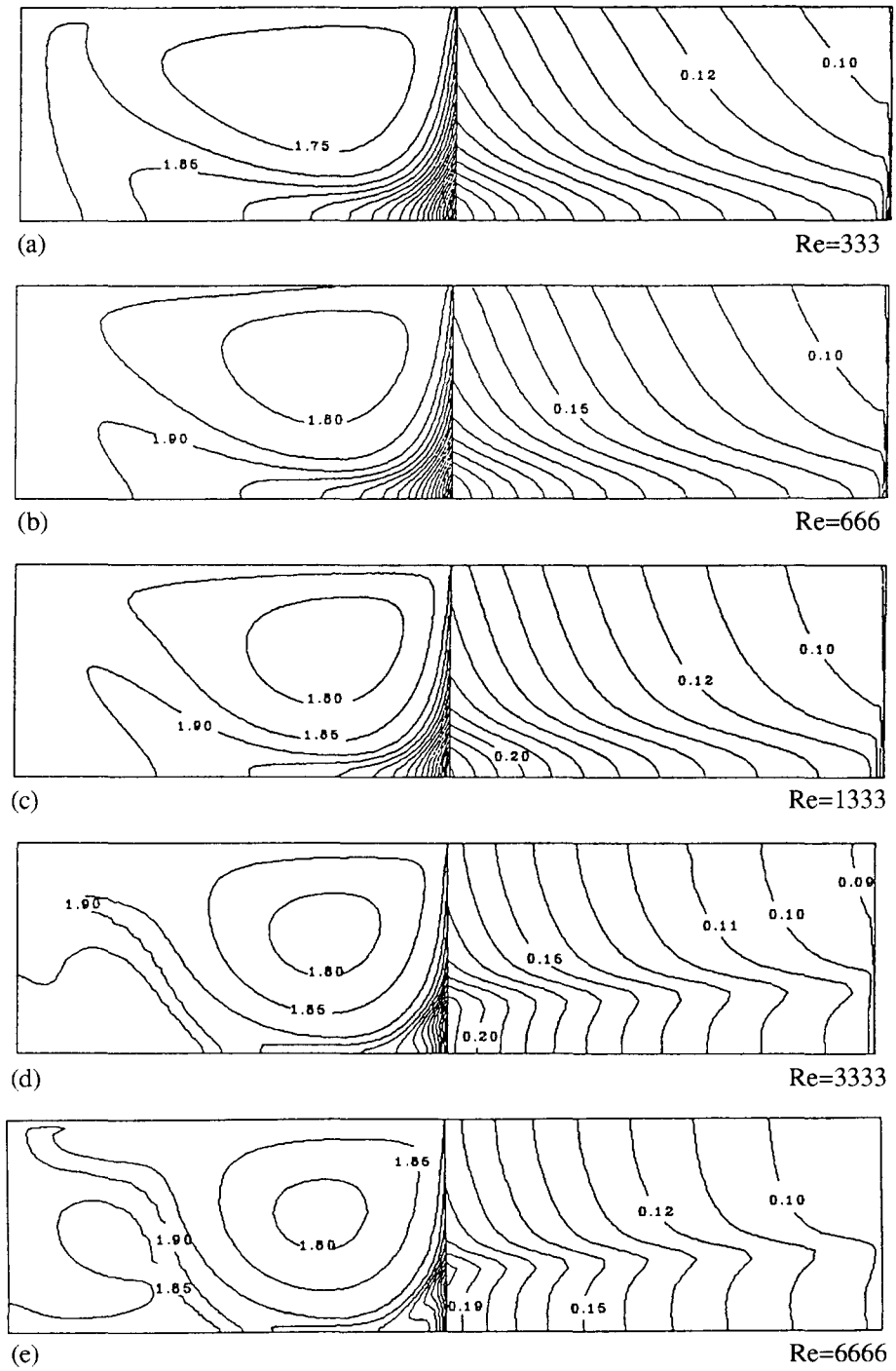

Fig. 5. Iso-concentration lines for Sc = 10 and different Reynolds numbers.

3.2. Open cavity: rigid–free case

3.2.1. Thermocapillary-driven convection

In the absence of gravity the buoyancy force vanishes (i.e., Gr = 0) and the flow is driven only by thermocapillary forces. We first consider the thermocapillary effects on the solidification process at increasing Reynolds numbers Re. The flow consists of a clockwise rotating cell which evolves with increasing Re towards a concentrated eddy located near the cold wall. Two more quiescent zones take place with increasing Re, in the bottom corners of the cavity. For more details, Ben Hadid and Roux [20] have carried out large computations to investigate the thermocapillary flow structure.

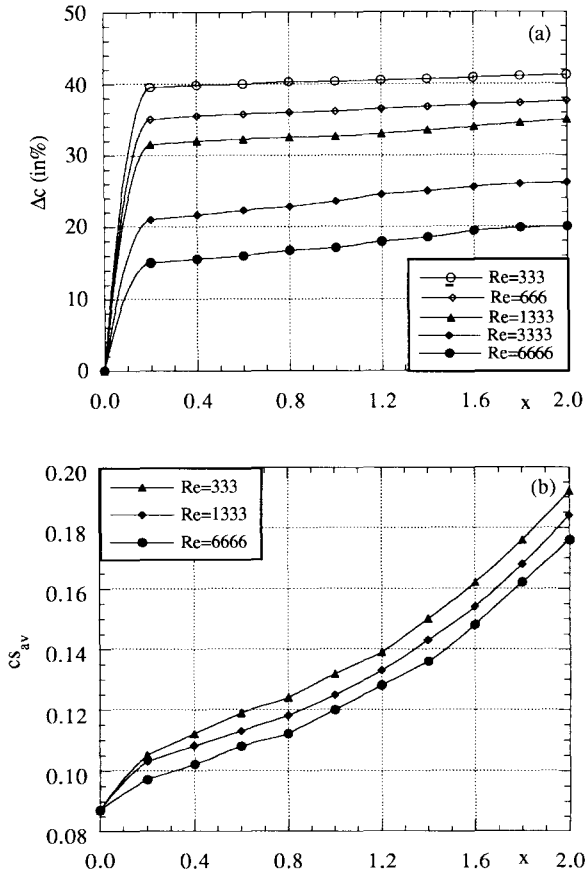

Fig. 6. Evolution of the radial segregation (a) and the longitudinal segregation (b) along the crystal axis for Sc = 10 and different Reynolds numbers.

In order to analyse the influence of the thermocapillary-driven flow on the dopant distribution, plots of concentration fields for Sc = 10 are shown in fig. 5. In the melt, the qualitative features of these fields are still the presence of two zones: an enriched solute boundary layer with steep gradients near the melt–crystal interface (caused by the dopant rejected by the crystal) and a region well mixed by the roll where the dopant concentration is much more uniform. The solute boundary layer is generally not uniform in depth: the depth increases from the top where the horizontal velocity is maximum because of the free surface, to the bottom where there is an enrichment because the dopant is transported by the descending flow along the interface. This gives for the crystal an increase of the dopant concentration from the top to the bottom with steep gradients in the lower zone (figs. 5a–5c). Specific behaviour occurs for large values of Re. First, the flow at the top of the interface is strong enough to sweep the dopant and create a thin but more uniform solute boundary layer: this gives nearly vertical concentration lines in the poor zone near the top of the crystal. Then, the contra-rotating roll in the right bottom corner becomes enough intensive to limit the enrichment in that zone: as a consequence a decrease of the dopant concentration in the crystal near the bottom is observed limiting the strong increase from the top to the bottom that was obtained previously.

As a further investigation concerning the influence of the melt flow on the dopant repartition, the radial segregation Δc and the longitudinal segregation cs_{av} along the crystal axis are displayed in fig. 6 for various Reynolds numbers. As shown in this figure, the values of radial segregation along the crystal axis decrease when the Reynolds number is increased (fig. 6a): this is due to the specific behaviour mentioned above which gave a better uniformity in the upper part of the crystal and a limitation of the enrichment in the lower part. Nevertheless, a higher level of mixing leads to a reduction of the global quantity of dopant contained in the crystal (fig. 6b). This behaviour can be related to the fact that when the Reynolds number increases, the strength of the velocity also increases and the flow close to

the melt–crystal interface carries more dopant away from the interface, reducing the enrichment of the crystal.

The concentration fields for Re = 333 and various Schmidt numbers ($1 \leq Sc \leq 100$) are displayed in fig. 7, providing a qualitative framework to analyse the effect of the diffusive mass transport mode on segregation during the solidification process. We have to recall that in our modellization (eqs. (1)–(5)) an increase of Sc decreases the solute diffusion compared to the solute transport by convection, but at the same time increases the solute gradient at the interface. In these figures, we may notice that for increasing values of the Schmidt number, the solute boundary layer close to the solidification interface shrinks and the dopant concentration in the core of the melt becomes more homogeneous. This behaviour may be related to the increasing effect of mixing by convection which drives the dopant

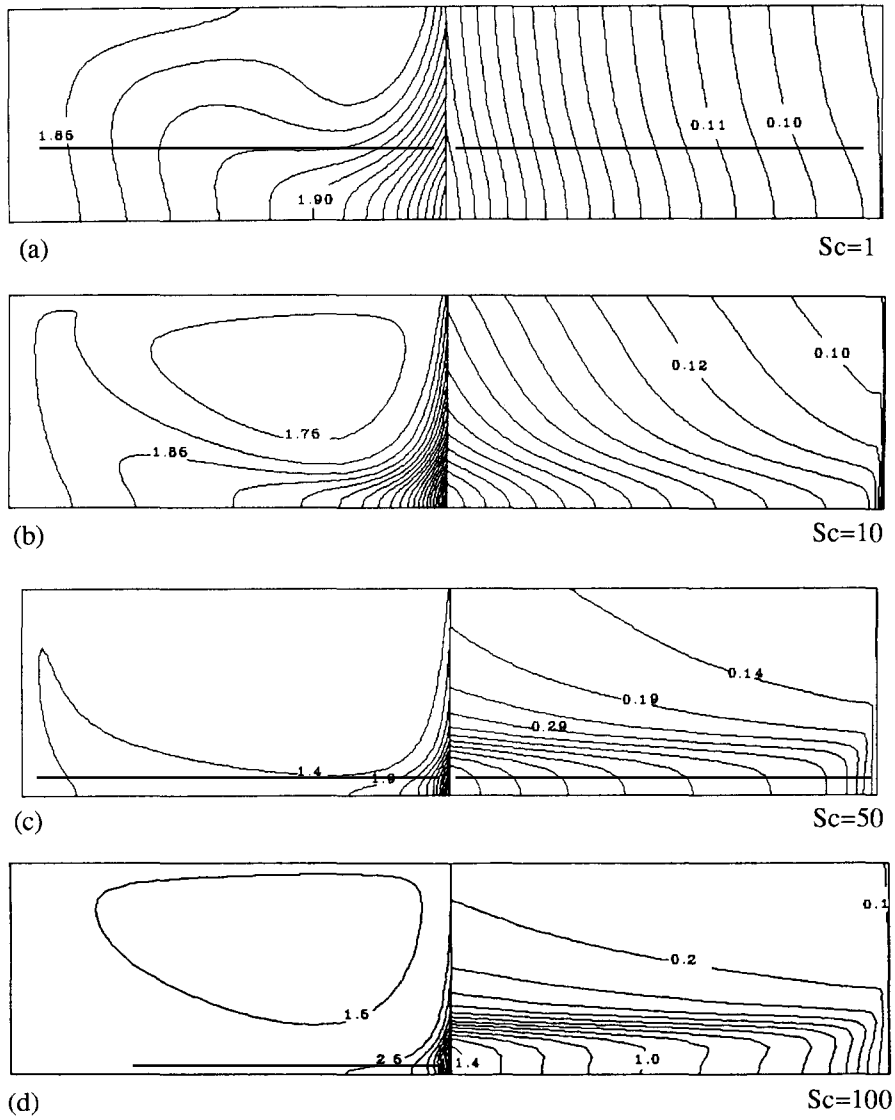

Fig. 7. Iso-concentration lines for Re = 333 and different Schmidt numbers.

distribution in the melt when the dopant diffusion becomes weaker (i.e., increasing Schmidt number). As for large Gr, the boundary layer extent is very thin and quite uniform near the top and increases strongly at the bottom in the quiescent zone of the right corner. But here, the well mixed upper zone of the melt is practically not enriched during the solidification process. This gives a crystal with a rather large quite uniform upper part, above a strongly enriched layer at the level of the quiescent zone. This enrichment is still limited near the bottom of the crystal by the effect of the contra-rotating roll at the right bottom corner of the melt.

For quantitative evaluation, we plot in fig. 8a the longitudinal segregation along the crystal axis for Re = 333 and different Schmidt numbers. In this figure, we may notice that the crystal contains more dopant when the Schmidt number increases. For instance, at the final state (i.e., $S = 2$), the global quantity of dopant contained in the crystal for the case Sc = 100 is 2.8 times more important than that for Sc = 1. This result indicates that as Sc is increased, the effect due to the rise of the dopant concentration gradient at the interface is preponderant compared to the effect due to a better level of mixing. On the other hand, the radial segregation increases strongly when Sc is increased. Indeed, its maximum goes from 6% for Sc = 1 to 265% for Sc = 100 (it equals 42% for Sc = 10 and 164% for Sc = 50). This is due to a stronger heterogeneity between the top and the bottom of the crystal. Its normalized form is plotted in fig. 8b as a function of the abscissa along the crystal axis for four values of the Schmidt number (Sc = 1, 10, 50 and 100). These curves indicate that for small Sc values ($1 \leq Sc \leq 10$), the radial segregation evolves more rapidly during the solidification process towards an almost constant value. This behaviour may be connected to the interference of the melt flow and the solute boundary layer: when the Schmidt number is decreased, the boundary layer is larger, and thus more rapidly disturbed by the flow.

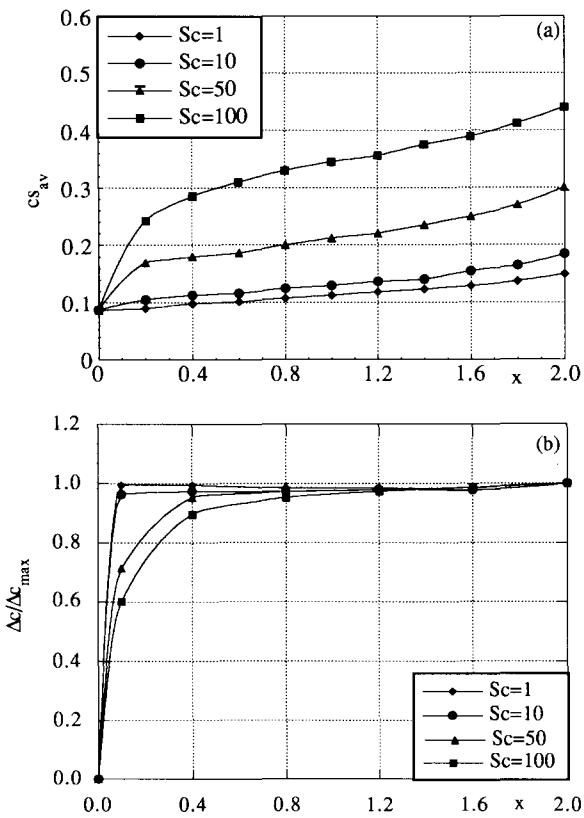

Fig. 8. Evolution of the longitudinal segregation (a) and the normalized radial segregation (b) along the crystal axis for Re = 333 and different Schmidt numbers.

Using the present results it can be argued that convective mass transfer plays a dominant role in the dopant distribution for increasing Schmidt number, even for moderate convective intensities.

3.2.2. *Effect of a magnetic field*

In this section, we focus on the effects induced by a constant magnetic field on the melt flow and the crystal structure. We investigate, first, the flow structure for values of Hartmann numbers Ha ranging up to 250. We present for $S = 2$, Re = 3333 and various Hartmann numbers the streamlines in fig. 9 and the vertical velocity profiles (at $x = 0.5$) in fig. 10. The effect of Ha on the flow is both quantitative and qualitative. The flow intensity is strongly reduced by the magnetic field (see fig. 10) and we may notice in fig. 9 a change in the flow structure. Indeed, the eddy disappears for $Ha \geq 50$ and the flow becomes parallel. The results are similar to those obtained for steady situations in fixed cavities (for an aspect ratio $A > 2$) by Ben Hadid et al. [21]. It is

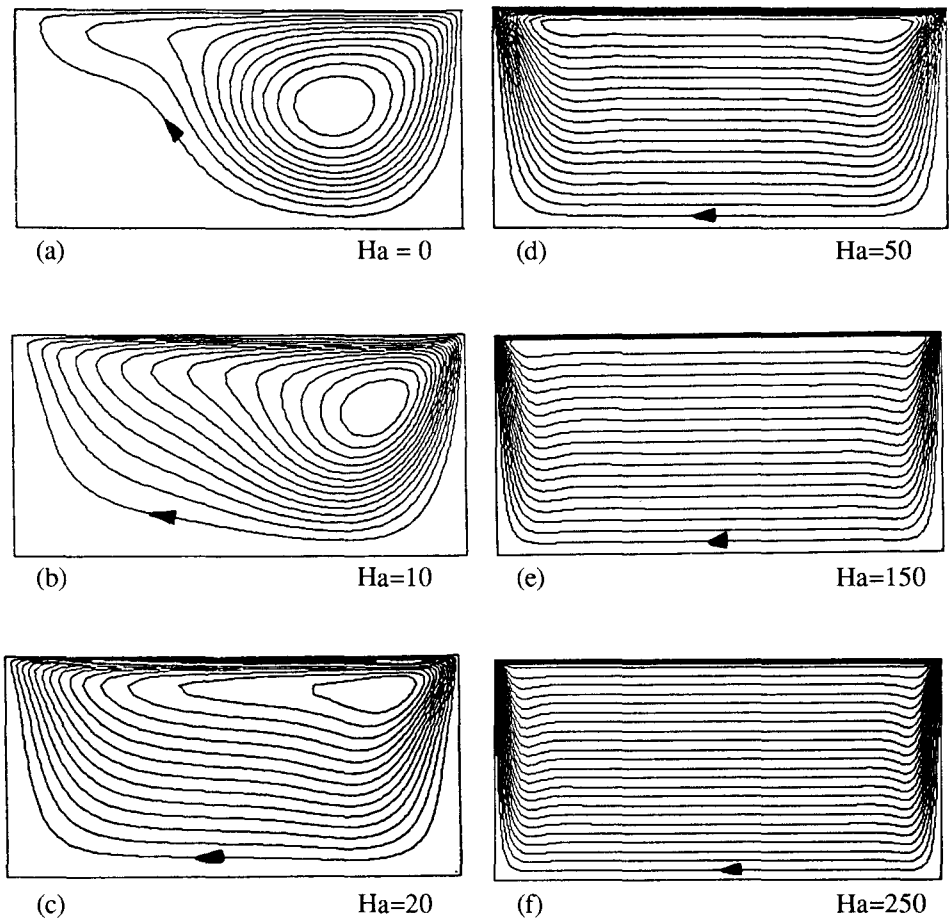

Fig. 9. Streamlines for Re = 3333, $S = 2$ and different Hartmann numbers.

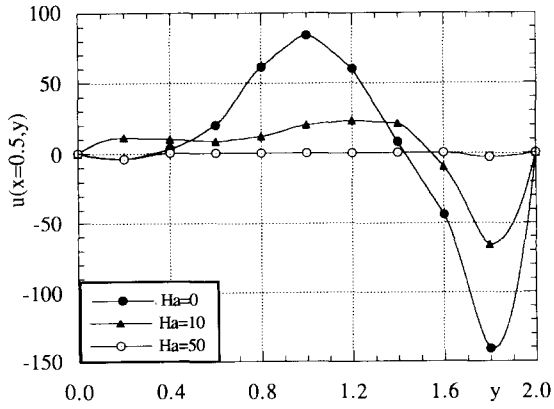

Fig. 10. Evolution of the vertical velocity component $u(x = 0.5, y)$.

shown that for high Ha the circulation near the free surface occurs on a small depth ($\sim \mathrm{Ha}^{-1}$) with a maximum velocity proportional to Ha^{-1}, whereas the returning flow occupies almost the whole depth of the cavity with a constant velocity proportional to Ha^{-2}.

As a consequence, when the Hartmann number is increased, the well-mixed zone disappears because of the strong reduction of the melt flow intensity and the distortion of the iso-concentration lines induced by the flow is strongly reduced. In figs. 11d and 11e, we may notice that the diffusive regime is approached for important values of Ha (Ha > 250) and the remaining deformations of the iso-concentration lines for these val-

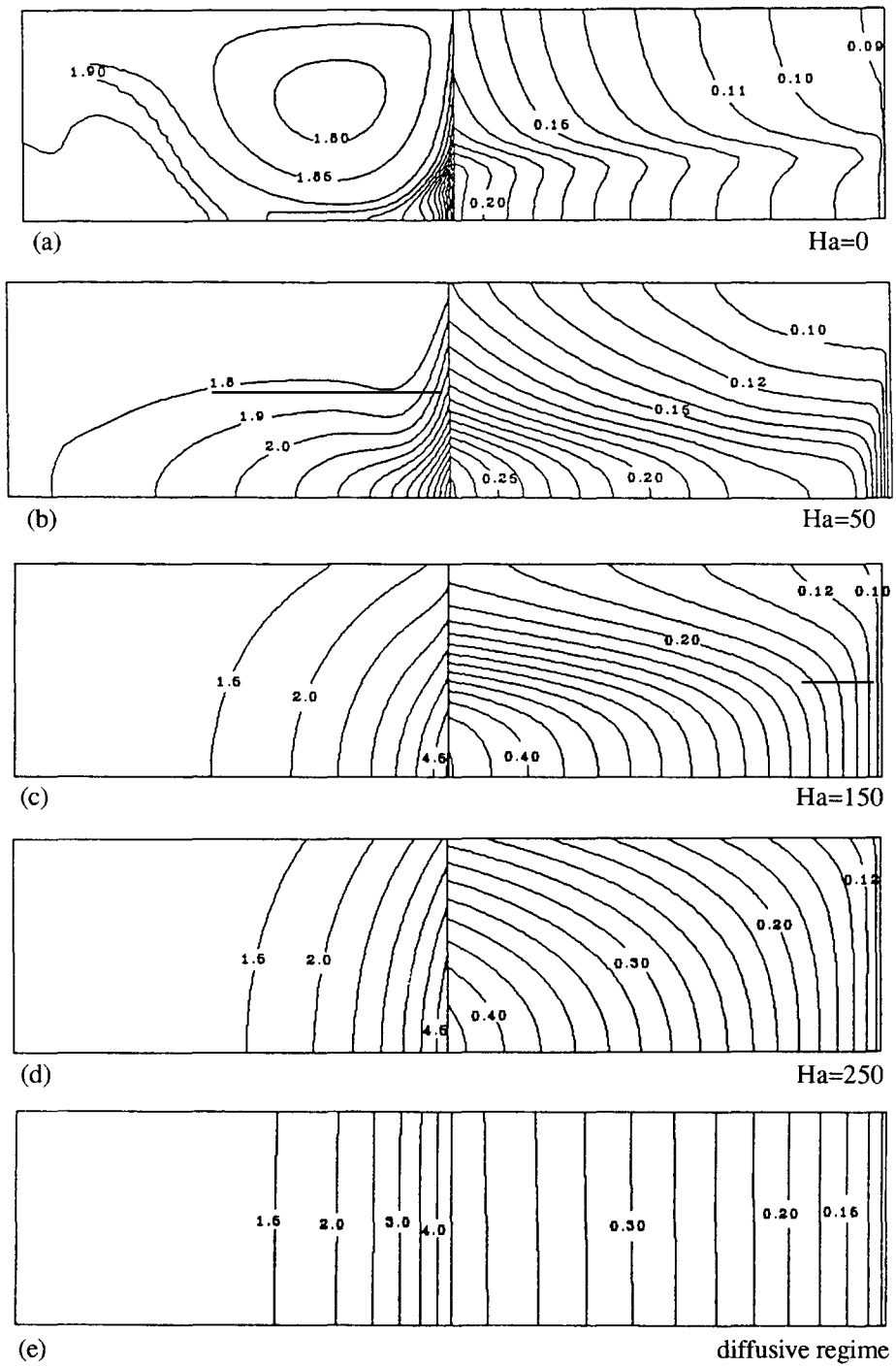

Fig. 11. Iso-concentration lines for Re = 3333, Sc = 10 and different Hartmann numbers.

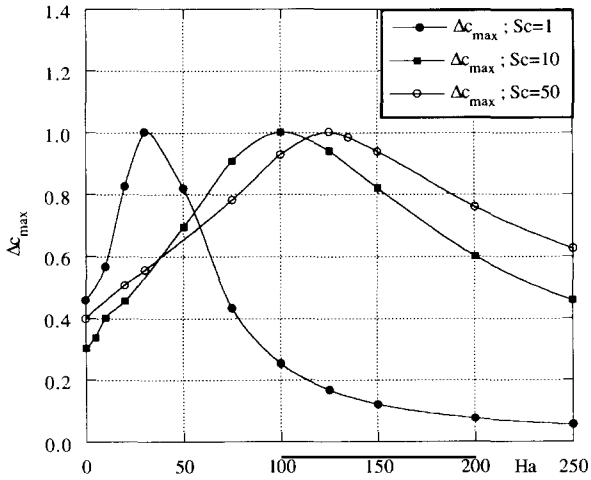

Fig. 12. Evolution of the maximum normalized radial segregation for different values of the Schmidt number as a function of the Hartmann number.

ues of Ha (close to a parabolic form) are typical of Marangoni flows submitted to a magnetic field and are found to be generated by the constant velocity returning flow (see [21]). In the crystal, with increasing Ha, the iso-concentration lines are first more elongated because of the disparition in the melt of the well mixed zone and of the small contra-rotating roll. Then, the distortion of the iso-concentration lines decreases gradually as the flow slows down, confirming the important role of the flow motion in defining the dopant repartition in the crystal (see fig. 11).

In fig. 12, the normalized maximum values of the radial segregation during the solidification process are plotted as a function of the Hartmann number for several values of the Schmidt number (Sc = 1, 10 and 50). The maximum values of these curves used for the normalization are around 9% for Sc = 1, 90% for Sc = 10 and 300% for Sc = 50. These maximums are reached for a critical Hartmann number Ha_c of 30, 100 and 125 for Sc = 1, 10 and 50, respectively. The critical Hartmann number corresponds to the worst radial segregation growth conditions for a given Schmidt number. These three curves have the same bell shape. In the first part of these curves ($Ha \leq Ha_c$), the maximum values of the radial segregation increase with the Hartmann number because the level of mixing is decreased. Then, beyond the critical Hartmann number ($Ha \geq Ha_c$), the maximum values of the radial segregation begin to decrease because the flow intensity is strongly damped, and the diffusion controlled regime is approached (for the diffusion controlled regime the radial segregation is zero). The approach of the diffusive regime is easier for low Schmidt number fluids (smaller Ha_c and steeper decrease of the curves). Such cases are less perturbed by the flow and are then more easily restored.

All these results reflect the strong sensitivity of the radial segregation in the crystal to the melt motion.

4. Conclusion

The purpose of this study was to analyse the effects of buoyancy and thermocapillary-driven convection on macrosegregation for the horizontal Bridgman configuration and to investigate numerically the solute boundary layer extent. The effects of a constant transverse magnetic field on the flow structure and on the dopant repartition were also investigated for a wide range of Hartmann numbers.

It appears that the melt convective motions have a great influence on macrosegregation. It has been shown that both flow structure and flow intensity influence the dopant concentration field in the melt and consequently affect the crystal quality. For buoyant flows, the thickness of the solute boundary layer has been estimated using the analytical expressions given by Favier [3,4] and the obtained results compare favourably with those of Garandet et al. [19].

Capillary-driven flows which are the dominating ones in space, can also considerably disturb the dopant distribution giving important radial segregation in the crystal. When applying a constant transverse magnetic field, the convective intensity is damped and the flow structure is considerably modified. These modifications of the flow have important effects on the dopant repartition both in the melt and in the crystal: the well mixed zones disappear and for low Schmidt num-

ber fluids ($Sc \leq 1$), the level of radial segregation is strongly reduced for important magnetic field intensity. It was also shown that the radial segregation has a maximum for intermediate field strength.

Acknowledgements

The authors would like to express their grateful thanks to Professor R. Moreau from MADYLAM of Grenoble and to Drs. J.P. Garandet and D. Camel from CEN, Grenoble, for helpful discussions. This work is supported by the CNES through the microgravity program. Computations were carried out on the Cray-2 computer, with support from the Centre de Calcul Vectoriel pour la Recherche (CCVR).

References

[1] V.G. Smith, W.A. Tiller and J.W. Rutter, Can. J. Phys. 33 (1955) 723.
[2] E. Scheil, Z. Metallk. 34 (1942) 70.
[3] J.J. Favier, Acta Met. 29 (1981) 197.
[4] J.J. Favier, Acta Met. 29 (1981) 205.
[5] D. Camel and J.J Favier, J. Crystal Growth 67 (1984) 42.
[6] D. Camel and J.J Favier, J. Crystal Growth 67 (1984) 57.
[7] J.D. Verhoeven, W.N. Gill, J.A. Puszynski and R.M. Ginde, J. Crystal Growth 89 (1988) 189.
[8] J.D. Verhoeven, W.N. Gill, J.A. Puszynski and R.M. Ginde, J. Crystal Growth 97 (1989) 254.
[9] C.J. Chang and R.A. Brown, J. Crystal Growth 63 (1983) 343.
[10] P.M. Adornato and R.A. Brown, J. Crystal Growth 80 (1987) 155.
[11] S.A. Nikitin, V.I. Polezhayev and A.I. Fedyushkin, J. Crystal Growth 52 (1981) 471.
[12] R.W. Series and D.J.T. Hurle, J. Crystal Growth 113 (1991) 305.
[13] M. Mihelčić and K. Wingerath, J. Crystal Growth 71 (1985) 163.
[14] D.H. Kim, P.M. Adornato and R.A. Brown, J. Crystal Growth 89 (1989) 339.
[15] R. Hirsh, J. Comput. Phys. 19 (1975) 90.
[16] B. Roux, P. Bontoux, T.P. Loc and O. Daube, Optimization of Hermitian methods for NS equations in vorticity streamfunction formulation, in: Lecture Notes in Mathematics, Vol. 771, Ed. R. Rautmann (Springer, Berlin, 1980) pp. 450–468.
[17] J.F. Thompson, Z. Vawarsi and C.W. Mastin, Numerical Grid Generation (Elsevier, Amsterdam, 1985).
[18] H. Ben Hadid, PhD Thesis, Université Aix–Marseille (1989).
[19] J.P. Garandet, T. Duffar and J.J. Favier, J. Crystal Growth 106 (1990) 437.
[20] H. Ben Hadid and B. Roux, J. Fluid Mech. 221 (1990) 77.
[21] H. Ben Hadid and D. Henry, to be published.